AGU PUBLICATIONS

JGR

Journal of Geophysical Research: Space Physics

RESEARCH ARTICLE

10.1002/2015JA021408

Upper *D* region chemical kinetic modeling of LORE relaxation times

F. J. Gordillo-Vázquez[1], A. Luque[1], and C. Haldoupis[2]

[1]Instituto de Astrofísica de Andalucía, CSIC, Granada, Spain, [2]Department of Physics, University of Crete, Heraklion, Greece

Key Points:
- Kinetics underlying LOng Recovery Early VLF events (LOREs) relaxation times
- Recombination of electron with hydrated cluster positive ions above 79-80 km controls LORE relaxation times
- Model-based results agree with recorded LORE recovery times

Correspondence to:
F. J. Gordillo-Vázquez,
vazquez@iaa.es

Citation:
Gordillo-Vázquez, F. J., A. Luque, and C. Haldoupis (2016), Upper *D* region chemical kinetic modeling of LORE relaxation times, *J. Geophys. Res. Space Physics*, *121*, 3525–3544, doi:10.1002/2015JA021408.

Received 30 APR 2015
Accepted 21 MAR 2016
Accepted article online 27 MAR 2016
Published online 15 APR 2016

Abstract The recovery times of upper *D* region electron density elevations, caused by lightning-induced electromagnetic pulses (EMP), are modeled. The work was motivated from the need to understand a recently identified narrowband VLF perturbation named LOREs, an acronym for *LOng Recovery Early VLF events*. LOREs associate with long-living electron density perturbations in the upper *D* region ionosphere; they are generated by strong EMP radiated from large peak current intensities of ±CG (cloud to ground) lightning discharges, known also to be capable of producing elves. Relaxation model scenarios are considered first for a weak enhancement in electron density and then for a much stronger one caused by an intense lightning EMP acting as an impulsive ionization source. The full nonequilibrium kinetic modeling of the perturbed mesosphere in the 76 to 92 km range during LORE-occurring conditions predicts that the electron density relaxation time is controlled by electron attachment at lower altitudes, whereas above 79 km attachment is balanced totally by associative electron detachment so that electron loss at these higher altitudes is controlled mainly by electron recombination with hydrated positive clusters $H^+(H_2O)_n$ and secondarily by dissociative recombination with NO^+ ions, a process which gradually dominates at altitudes >88 km. The calculated recovery times agree fairly well with LORE observations. In addition, a simplified (quasi-analytic) model build for the key charged species and chemical reactions is applied, which arrives at similar results with those of the full kinetic model. Finally, the modeled recovery estimates for lower altitudes, that is <79 km, are in good agreement with the observed short recovery times of typical early VLF events, which are known to be associated with sprites.

1. Introduction

LOng Recovery Early VLF events (LOREs) represent a small subclass of early VLF events which associate with direct tropospheric lightning effects on the mesosphere and lower ionosphere caused by induced quasi-electrostatic (QE) and electromagnetic pulsed (EMP) fields. These direct lightning interactions may lead to ionospheric conductivity modifications which affect VLF transmissions propagating in the Earth-ionosphere waveguide and the generation of various types of momentary optical emissions known as *transient luminous events* (TLE). The most common TLE categories are those of *sprites* and *elves*, which have their origin in lightning QE and EMP field effects in the upper atmosphere, respectively [*Pasko et al.*, 2012, and references therein].

Typical early VLF events are abrupt perturbations in amplitude and phase of narrowband VLF signal receptions. They occur within ~20 ms of a causative lightning discharge having either a fast (<20 ms) or slow (~1 or 2 s) onset duration and typical recoveries in the range from ~50 to 180 s [see *Inan et al.*, 1996; also *Inan et al.*, 2010, and references therein].

Early VLF events have been studied extensively in an effort to understand their relation to TLEs, an issue that has been surrounded in earlier studies by controversy. In an effort to resolve this controversy, *Haldoupis et al.* [2004] and *Neubert et al.* [2005] used multi-instrument observations in Europe to obtain convincing evidence in favor of a close relationship between sprites and early VLF perturbations, suggesting a nearly one-to-one association. These findings prompted *Marshall et al.* [2006] to test this relationship further by analyzing a data set of concurrent sprite and early VLF events. Their results suggested that sprites and early VLF events were related, but not in a one-to-one correlation; that is, they found that about 48% of early events were associated with sprites. In discussing the difference between the two data sets, *Marshall et al.* [2006] suggested that these might be due to the relative location of the causative lightning along the VLF signal path (i.e., near transmitter or near receiver) in that mode coupling of the propagating VLF signal causes some perturbations

to be undetectable at long distances from the disturbed region. The whole issue and its disagreements were dealt with in a detailed study by *Haldoupis et al.* [2010]. This latest study confirmed that visible sprite occurrences are accompanied by early event perturbations in a one-to-one correspondence, but this relationship, if viewed conversely, appeared not to be always reciprocal, which suggested a possible role also for the so-called subvisual sprites, e.g., see *Pasko* [2010].

In the light of the above observations, one likely reason for the early-type VLF perturbations is the production of ionization at sprite altitudes driven by QE fields induced by +CG lightning with large charge moment changes leading to sprite discharges, as well as sprite halos [*Pasko et al.*, 2012]. In this case then, the observed early event recoveries of tens of seconds can be understood in terms of anticipated electron density relaxation times at sprite and sprite halo altitudes, typically below 80 km, between about 60 km and 85 km, as shown by *Haldoupis et al.* [2009].

The present paper aims in explaining the long recoveries of LOREs, which have been identified first by *Cotts and Inan* [2007] as a distinct VLF signature caused by lightning. While LOREs have abrupt onsets and onset duration similar to those of typical early VLF events, they differ from them by their long recoveries, which range from several minutes up to ~20 to 30 min, or even longer. The origin of LOREs was experimentally identified in the studies by *Haldoupis et al.* [2012, 2013] and *Salut et al.* [2012, 2013], to be associated with unusually large peak currents of CG lightning discharges.

Multi-instrument data sets showed that LOREs are triggered by powerful CG lightning discharges of either positive or negative (±) polarity, carrying very large peak currents (>250 kA) which are also capable of producing elves or elve-sprite pairs, especially if the causative CG discharge polarity was positive. The observations suggested that LOREs are caused by lightning-emitted, strong electromagnetic pulsed (EMP) electric fields which impact onto the upper mesosphere, at heights >80 to ~85 km, to generate long-lasting elevations in electron density. In addition, it was implied that LORE is the VLF fingerprint of elves, a fact that was predicted by EMP theory earlier [*Rodger*, 2003]. Certainly, one cannot exclude the option that LOREs may also associate with elevations in ionization which occur in relation with high altitude sprite halos or halos alone, with the latter occurring with either positive or negative CG lighting discharges [e.g., *Newsome and Inan*, 2010; *Williams et al.*, 2012]. Still, however, this latter option remains to be verified by observations.

This paper continues research on LOREs by taking a closer look at their long recoveries. It presents theory estimates and modeling results, which provide a better physical understanding of the phenomenon, and helps quantify lightning EMP effects on electron density production and relaxation in the nighttime upper *D* region ionosphere. In the following, a full nonequilibrium kinetic model of air plasmas is used first to compute the relaxation times of a weakly enhanced (above ambient values) electron density perturbation at upper *D* region heights. Next, a two dimensional (2-D) EMP model is employed to compute the EMP electric fields causing strong ionization enhancements by electron impact in the upper *D* region that is representative of LORE-occurring conditions. Next, these fields are used in the full nonequilibrium kinetic model of the air plasmas to independently predict electron density relaxation times and identify the prevailing kinetic paths during and after the action of intense lightning EMP fields associated with elves. Finally, a simplified kinetic model is presented and used to explain physically the fundamental kinetic processes and their corresponding time scales which determine the LORE relaxation times of electron density enhancements in the upper *D* region.

Before presenting the model and its findings, a brief reference is made first, for completeness purposes, on LORE observational characteristics. These are summarized below.

2. LORE Observational Properties

The present LORE knowledge and experimental properties are documented in two recent papers by *Haldoupis et al.* [2013] and *Salut et al.* [2013]. Both are statistical studies of early-type VLF perturbations occurring in relation with intense CG lightning discharges with peak currents > | ± 200| kA. It should be noted that there is recent support for an elve production cutoff of ≃88 kA peak current [*Blaes et al.*, 2016]. Previous elve production cutoff peak currents were established to ≃56 kA [*Barrington-Leigh and Inan*, 1999] and ≃60 kA [*Chen et al.*, 2008]. However, LORE occurrences increase with stroke current intensities and approach unity for discharges with peak currents greater than about |±300| kA. LORE perturbations are detected when a causative lightning discharge is located within ~250 to 300 km of the great circle path (GCP) of a VLF transmitter-receiver link,

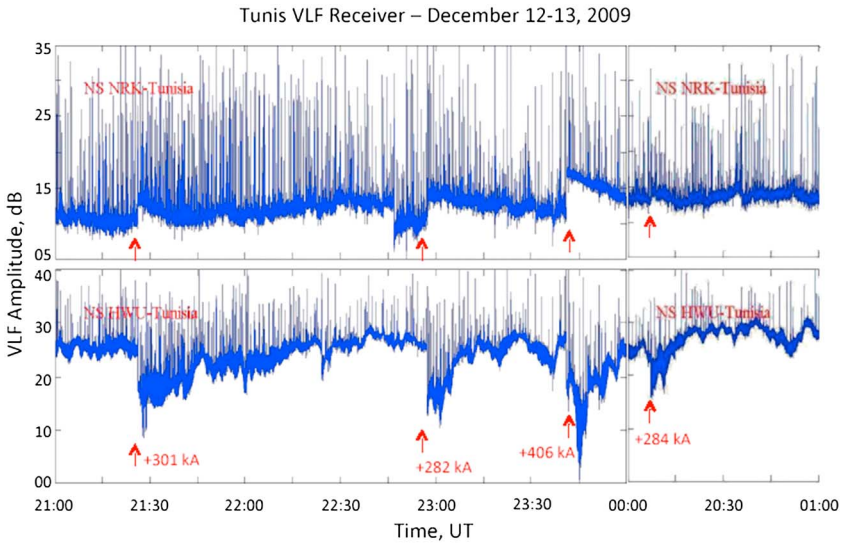

Figure 1. Long recovery early VLF event (LORE) occurrences associate with the most pronounced VLF perturbations caused by intense lightning discharge peak currents. See text for more details.

which implies a large perturbed area comparable with that of elves. They associate with the strongest and longest-living VLF perturbations caused by CG lightning discharges in the *D* region ionosphere.

The LORE phenomenon can be appreciated in Figure 1. It shows VLF recordings obtained with a Stanford receiver [*Cohen et al.*, 2010] located in Tunis, for two VLF links whose transmitter to receiver GCPs passed near a localized but very intense maritime storm located west of Corsica, at ~42°N and 7.5°E. The storm lasted ~6 h during the night of 12–13 December 2009, from ~21 to 03 h UT, and produced many TLE events, which included tens of sprites, several spectacular sprite-elve pairs, and a gigantic jet, the first ever to be observed in Europe [*van der Velde et al.*, 2010]. It also produced several strong +CG discharges with peak currents exceeding +250 kA, captured by the Italian LINET lightning detection system [*Betz et al.*, 2004], which produced LOREs concurrently with sprites and elves.

Figure 1 shows unfiltered (raw) signal amplitude time series, for the NRK (Island)-Tunis (top) and HWU (north France)-Tunis (bottom) VLF propagation links, recorded during a 4 h storm interval from 21 to 01 UT. Besides the dense sequence of numerous strong sferics caused by CG lightning, the most conspicuous perturbations in Figure 1 are those of LOREs, characterized by large sudden onsets and long recoveries to pre-event levels, exceeding in a few cases 30 min. The red arrows near onset indicate the occurrence of four prominent LORE events during this time interval, all triggered by unusually intense +CG discharges with peak currents ranging from +282 to +406 kA.

Since the present paper deals with the modeling of LORE recoveries, it is important to have information about their dependence on causative peak current intensities. To measure the event recovery, however, is a formidable task in most cases because, as pointed out by *Haldoupis et al.* [2013] and *Salut et al.* [2013] and as it can also be inferred from Figure 1, it is difficult to get reliable recovery estimates due to additional ionospheric fluctuations occurring independently, which affect and complicate the signal on time scales of minutes. Despite this difficulty, an effort was made to manually reinspect the large data base used by *Haldoupis et al.* [2013] in order to identify typical LORE cases for which reasonable recovery estimates were possible within an approximate error bound of ~20%. The recovery time was defined here as the time between the event onset and the approximate moment when the signal returned to its pre-event level. Shown in Figure 2 are examples of such events caused by either a positive or negative CG discharge whose peak currents in kiloampere are denoted in red. Plotted are logarithmic VLF amplitudes of raw signal (unfiltered) recordings in which the recovery times, measured from the event onset to the time the signal relaxes back to its preonset level, are indicated in each plot by a line and the estimated recovery time, τ, in minutes.

Figure 3 summarizes in a point scatter plot the LORE recovery estimates versus their causative peak current intensities. It is based on 136 LORE events similar to those of Figure 2, with the majority of them (~70%)

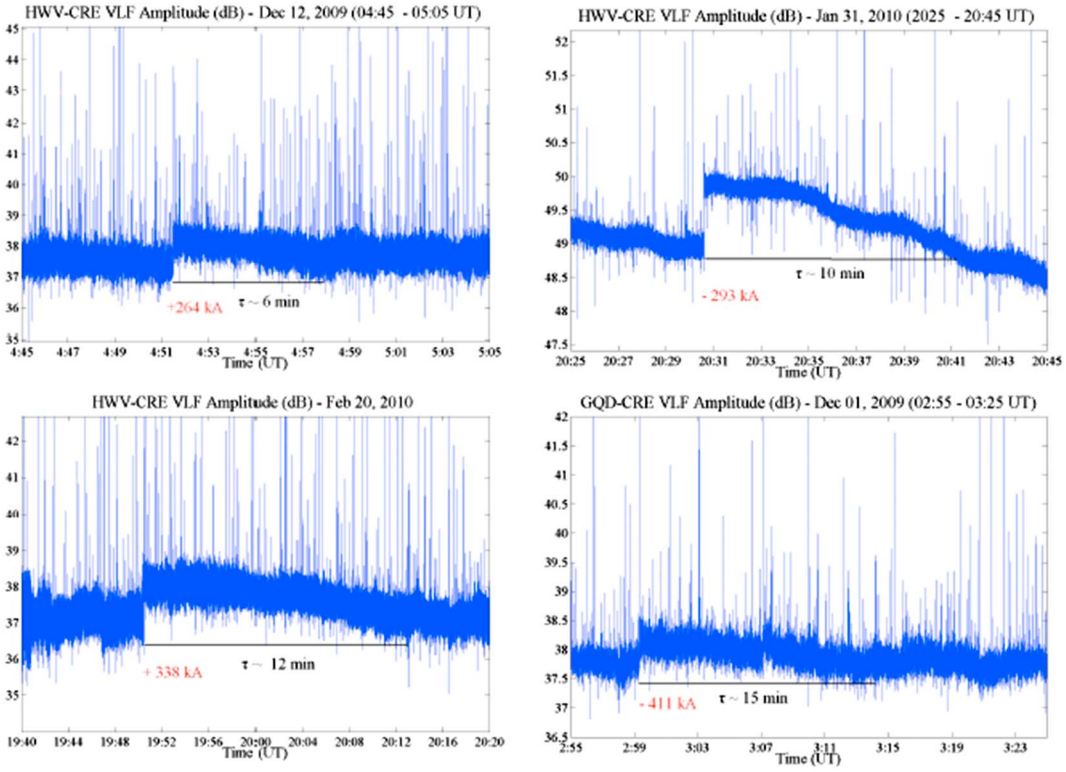

Figure 2. Typical examples of LOREs observed with the Crete VLF receiver, for which the event duration (recovery) can be estimated within a reasonable error bound.

belonging in the +CG lightning discharge group marked with red dots in Figure 3, while the blue dots denote −CG strokes. As seen, there is a clear trend for the LORE recoveries to increase with stroke peak current. The observed dependence was fitted by a straight line that produced a linear correlation coefficient of ~75%. A similar effort for the LORE onset amplitudes measured in decibels did not produce any obvious trend or a functional relationship with the causative peak currents, which is in agreement with a similar conclusion made by *Salut et al.* [2013]. The lack of LORE amplitude dependence on peak current can be attributed to various unresolved signal complexities. These may include VLF modal propagation effects on the narrowband VLF amplitude and phase at the receiver, uncertainties in the altitude and horizontal extent of the effective scattering region, and obscure signal variations caused by irregular changes in the state of the nighttime *D* region ionosphere along the entire great circle path from the transmitter to the receiver.

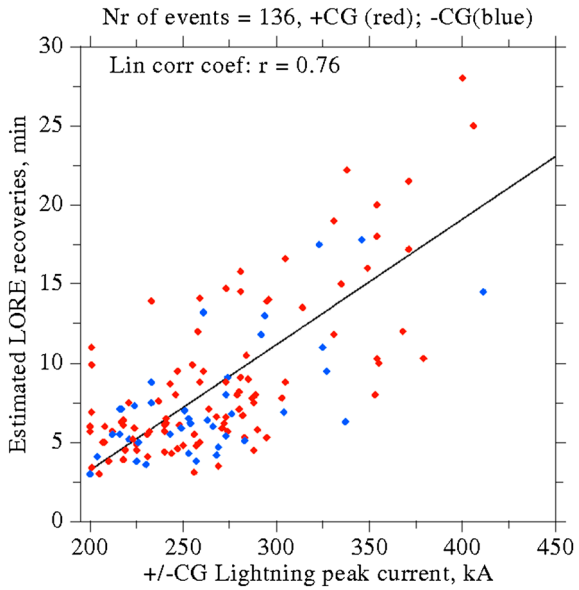

Figure 3. Dependence of estimated LORE recovery times on the causative CG lightning discharge peak current for both positive (red) and negative (blue) current polarities. There is a linear trend which is fitted by a straight line with a linear correlation coefficient of 0.76.

3. Modeling the LORE Recoveries

The key hypothesis adopted here, which relies on strong experimental evidence, is that LOREs are due to VLF scattering from electron density enhancements caused by lightning-induced EMPs, impacting onto

Table 1. Mitra-Rowe Scheme Implemented in This Study Following the Work By *Mitra* [1975][a]

Reaction	Rate Coefficient
$NO^+ \rightarrow H^+(H_2O)_n$	$B = 1.0 \times 10^{-31} N^2$ s^{-1}
$O_2^+ \rightarrow H^+(H_2O)_n$	$B = 1.0 \times 10^{-31} N^2$ s^{-1}
$O_4^+ \rightarrow H^+(H_2O)_n$	$B = 1.0 \times 10^{-31} N^2$ s^{-1}
$e + H^+(H_2O)_n \rightarrow$ Neutrals	$\alpha_d^c = 1.0 \times 10^{-5}$ cm^3 s^{-1}
$O_2^- + H^+(H_2O)_n \rightarrow$ Neutrals	$\alpha_i = 1.0 \times 10^{-7}$ cm^3 s^{-1}
$CO_3^- + H^+(H_2O)_n \rightarrow$ Neutrals	$\alpha_i = 1.0 \times 10^{-7}$ cm^3 s^{-1}

[a]The parameter N stands for the total gas density (in cm^{-3}) at different altitudes.

the uppermost *D* region ionosphere. In all theoretical and numerical simulation studies of lightning EMP-ionosphere interaction [see *Marshall*, 2012, and references therein], EMP effects produce excitation of optical emissions (elves) and electron density elevations at altitudes above ~75 to 80 km. In the following, the altitudes under consideration are confined in with upper *D* region ionosphere, in the range from 76 to 92 km, which of course does not necessarily imply that VLF transmissions reach all the way up to this upper altitude. Given that at regular nighttime conditions VLF signals reflect near 85 ± 2 km, the reflection heights during LOREs are expected to become lower because of the anticipated elevations in electron density also below the regular reflection heights. Therefore, the relaxation of the lightning-induced electron density elevations suggests that VLF signals reflect over a range of heights during LORE lifetimes. This is expected because, as it will be shown later, the effective reflection height is likely to increase with time during the event, because the ionization relaxes to ambient levels faster at lower rather than at higher altitudes.

3.1. Kinetic Modeling of LORE Relaxation Times

The full nonequilibrium kinetic model of air plasmas proposed by *Gordillo-Vázquez* [2008, 2010], *Gordillo-Vázquez and Luque* [2010], and *Gordillo-Vázquez et al.* [2011, 2012] is used here for the study of the air plasma reaction kinetics during TLE occurrences in the Earth mesosphere and *D* region ionosphere. The basic model equations entering the nonequilibrium air plasma chemistry are a set of time-dependent continuity equations for each of the species involved, that is, ground neutrals, electronically, and vibrationally excited neutrals, as well as positive and negative atomic and molecular ions, and electrons. The model also treats the *D* region kinetics of positive cluster (hydrated) ions of the series $H^+(H_2O)_n$ lumped together in a Mitra-Rowe (M-R) scheme, originally proposed for solar flare studies [*Mitra and Rowe*, 1972]. The implemented M-R scheme, which is shown in Table 1, considers (a) the conversion of positive ions (NO^+, O_2^+, …) into positive cluster ions $H^+(H_2O)_n$ with an effective rate of conversion $B = 10^{-31} N^2$ s^{-1} where N stands for the total gas density at different altitudes and the fitted values of B follow very closely the observational data (ratio Σ $H^+(H_2O)_n$ / NO^+) between 70 km and 88 km, (b) the recombination of electrons with $H^+(H_2O)_n$ with an effective rate coefficient $\alpha_d^c = 10^{-5}$ cm^3 s^{-1} [*Mitra*, 1975], and (c) the recombination of negative ions (O_2^-, CO_3^-, …)

Table 2. Reduced Humid Chemistry Considered in the Full Kinetic Model[a]

Reaction	Rate Coefficient	Reference
$O(^1D) + H_2O \rightarrow OH + OH$	$2.2 \times 10^{-10} \left(\frac{T}{300}\right)^{0.5}$ cm^3 s^{-1}	*Brasseur and Solomon* [1986]
$H + O_2 + N_2 \rightarrow HO_2 + N_2$	$5.5 \times 10^{-32} \times \left(\frac{300}{T}\right)^{1.6}$ cm^3 s^{-1}	*Brasseur and Solomon* [1986]
$OH + O \rightarrow H + O_2$	$2.2 \times 10^{-11} \times \exp(117/T)$ cm^3 s^{-1}	*Brasseur and Solomon* [1986]
$OH + CO \rightarrow H + CO_2$	1.5×10^{-13} cm^3 s^{-1}	*Brasseur and Solomon* [1986]
$OH + O_3 \rightarrow HO_2 + O_2$	$1.6 \times 10^{-12} \times \exp(-940/T)$ cm^3 s^{-1}	*Brasseur and Solomon* [1986]
$H + O_3 \rightarrow OH^* + O_2$	$1.4 \times 10^{-10} \times \exp(-470/T)$ cm^3 s^{-1}	*Brasseur and Solomon* [1986]
$HO_2 + O_3 \rightarrow OH + O_2 + O_2$	$1.4 \times 10^{-14} \times \exp(-580/T)$ cm^3 s^{-1}	*Brasseur and Solomon* [1986]
$HO_2 + O \rightarrow OH + O_2$	$3.0 \times 10^{-11} \times \exp(200/T)$ cm^3 s^{-1}	*Brasseur and Solomon* [1986]
$HO_2 + OH \rightarrow H_2O + O_2$	$1.7 \times 10^{-11} \times \exp(416/T)$ cm^3 s^{-1}	*Brasseur and Solomon* [1986]
$HO_2 + NO \rightarrow NO_2 + OH$	$3.7 \times 10^{-12} \times \exp(240/T)$ cm^3 s^{-1}	*Brasseur and Solomon* [1986]
$HO_2 + HO_2 \rightarrow H_2O_2 + O_2$	$2.3 \times 10^{-13} \times \exp(590/T)$ cm^3 s^{-1}	*Brasseur and Solomon* [1986]
$H_2O_2 + OH \rightarrow HO_2 + H_2O$	$3.1 \times 10^{-12} \times \exp(-187/T)$ cm^3 s^{-1}	*Brasseur and Solomon* [1986]
$H_2O_2 + O \rightarrow OH + HO_2$	$1.4 \times 10^{-12} \times \exp(-2000/T)$ cm^3 s^{-1}	*Brasseur and Solomon* [1986]

[a]The gas temperature (T) is in kelvin.

Table 3. Reactions Added to the Kinetic Scheme in *Gordillo-Vázquez* [2008, 2010][a]

Reaction	Rate Coefficient	Reference
$N_2 + h\nu \rightarrow N_2^+ + e$	$T_{CR} / 2N\ s^{-1}$	*Thomas* [1974]
$O_2 + h\nu \rightarrow N_2^+ + e$	$T_{CR} / 2N\ s^{-1}$	*Thomas* [1974]
$N_2 + N_2O_2^+ \rightarrow O_2^+ + N_2 + N_2$	$1.1 \times 10^{-6} \left(\frac{300}{T}\right)^{5.3} \exp(-2357/T)\ cm^3\ s^{-1}$	*Kossyi et al.* [1992]
$O_2 + N_2O_2^+ \rightarrow O_4^+ + N_2$	$10^{-9}\ cm^3\ s^{-1}$	*Kossyi et al.* [1992]
$O_2^- + O_2 + N_2 / O_2 \rightarrow O_4^- + N_2 / O_2$	$3.5 \times 10^{-31} \left(\frac{300}{T}\right) cm^6\ s^{-1}$	*Thomas* [1974]
$O_2^- + NO_3 \rightarrow O_2 + NO_3^-$	$5 \times 10^{-10}\ cm^3\ s^{-1}$	*Kossyi et al.* [1992]
$O_2^- + N_2O \rightarrow N_2 + O_3^-$	$5 \times 10^{-13}\ cm^3\ s^{-1}$	*Kossyi et al.* [1992]
$O^- + O_2 + N_2 \rightarrow N_2 + O_3^-$	$1.1 \times 10^{-30} \left(\frac{300}{T}\right) cm^6\ s^{-1}$	*Capitelli et al.* [2000]
$O^- + NO + N_2/O_2 \rightarrow NO_2^- + N_2 / O_2$	$10^{-29}\ cm^6\ s^{-1}$	*Capitelli et al.* [2000]
$O^- + CO_2 + N_2/O_2 \rightarrow CO_3^- + N_2 / O_2$	$3.1 \times 10^{-28} \left(\frac{T}{300}\right)^{0.5} cm^6\ s^{-1}$	*Brasseur and Solomon* [1986]
$e + N_2O_2^+ \rightarrow O_2 + N_2$	$1.3 \times 10^{-6} \left(\frac{300}{T_e}\right)^{0.5} cm^3\ s^{-1}$	*Kossyi et al.* [1992]
$e + O_2 + O_2 \rightarrow O_2^- + O_2$	$1.4 \times 10^{-29} \left(\frac{300}{T_e}\right) \exp\left(\frac{-600}{T}\right) \exp\left(\frac{700(T_e - T)}{T_e T}\right) cm^6\ s^{-1}$	*Kossyi et al.* [1992]
$e + O_2 + N_2 \rightarrow O_2^- + N_2$	$1.07 \times 10^{-31} \left(\frac{300}{T_e}\right)^2 \exp\left(\frac{-70}{T}\right) \exp\left(\frac{1500(T_e - T)}{T_e T}\right) cm^6\ s^{-1}$	*Kossyi et al.* [1992]

[a]We have considered the ion pair production rate $T_{CR}\ cm^{-3}\ s^{-1}$ (due to different ionizing mechanisms at the different altitudes considered) reported by *Thomas* [1974] for the quite nighttime *D* region. *N* stands for the total gas density at the different altitudes. The gas and electron temperatures, *T* and T_e, are in kelvin.

and $H^+(H_2O)_n$ with an effective rate coefficient $\alpha_i = 10^{-7}\ cm^3\ s^{-1}$ [*Mitra*, 1975]. All these continuity equations are coupled to the time-dependent spatially uniform Boltzmann equation of the energy distribution function of free electrons in the mesospheric plasma.

The model considers more than 100 chemical species and about 1000 reactions including electron production mechanisms such as electron impact ionization and associative electron detachment [*Luque and Gordillo-Vázquez*, 2011], and electron loss processes due to attachment and dissociative recombination [*Gordillo-Vázquez*, 2008, 2010; *Parra-Rojas et al.*, 2013, 2015]. The whole set of humid chemistry reactions introduced first by *Gordillo-Vázquez* [2008] is replaced here by a reduced set of 13 kinetic mechanisms listed in Table 2, which involve atomic hydrogen (H), hydroxyl (OH) and H_2O, HO_2, and H_2O_2. Moreover, Table 3 shows the set of new processes that have been added to the air kinetic model scheme of *Gordillo-Vázquez* [2008].

The simulation process consisted of two steps. The first step considered the relaxation of the air kinetic scheme [*Sentman et al.*, 2008; *Parra-Rojas et al.*, 2013] in the absence of lightning activity. In order to exclude the effects of lightning and/or TLEs in the mesospheric chemical environment, the chemical equilibrium was examined for the dominant ion pair production rates due to different ambient ionizing mechanisms at various altitudes, adopted directly in this model from *Thomas* [1974] for the quiet nighttime *D* region ionosphere. In this scheme, the values of the ambient species concentrations at each altitude, including those of electrons and ions, were determined from their consistency with the ion pair production rate obtained when the model equations are left to evolve for a relatively long time ($t \sim 10^4$ s) in the presence of a fair weather reduced electric field $E/N = 0.005$ Td, which is typical at mesospheric altitudes [*Rakov and Uman*, 2003]. The initial ambient concentrations of the neutral species for dry air and for H_2O, H, OH, … at each altitude were taken from the Whole Atmosphere Community Climate Model (WACCM) [*Marsh et al.*, 2013] assuming midlatitude nighttime conditions at the same gas and electron temperature (~216 K). The densities of all species, including those of the neutrals and positive cluster ions $H^+(H_2O)_n$, obtained soon after the relaxation of the present air kinetic scheme were used as the new ambient concentrations to initialize the subsequent LORE kinetic simulations, in order to be consistent with the ion pair production rate that is adopted for the nighttime *D* region.

Figure 4 compares the original WACCM midlatitude nighttime ambient concentrations (solid lines) for atomic oxygen (O), ozone (O_3), and carbon monoxide (CO), with the concentrations of the same species resulting from the relaxation of the nighttime air kinetic scheme (dashed lines) between 76 and 92 km. Also shown are available measurements of nighttime ozone concentrations at midlatitude (crosses, CRISTA 1 ozone mean profiles [*Kaufmann et al.*, 2003]) and at equatorial latitudes (solid circles, SABER ozone profiles [*Smith et al.*, 2008]).

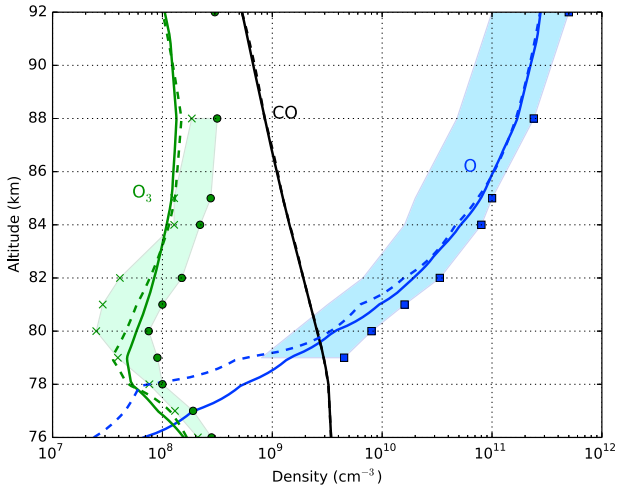

Figure 4. Ambient number density profiles of atomic oxygen (O), ozone (O_3), and carbon monoxide (CO) in the altitude range from 76 to 92 km. Solid lines are values produced by the WACCM model, while the dashed line curves correspond to the relaxed number densities obtained with the air kinetic model used in this investigation for upper atmospheric electrical discharges. Also shown are available measurements of nighttime ozone concentrations at midlatitude (crosses, CRISTA 1 ozone mean profiles [*Kaufmann et al.*, 2003]) and the equatorial region (solid circles, SABER ozone profiles [*Smith et al.*, 2008]). The green shaded region indicates the variability in the measurements of mesospheric nighttime ozone densities between middle and equatorial latitudes. The solid squares represent recent nighttime global atomic oxygen concentrations, derived from Sounding of the Atmosphere Using Broadband Emission Radiometry (SABER) observations in the upper mesosphere (79–100 km) [*Smith et al.*, 2010] and averaged over all latitudes. The blue shaded region indicates the variability of nighttime atomic oxygen density profiles which are based on past measurements [*Russell et al.*, 2005].

The green shaded region indicates the variability in the measurements of mesospheric nighttime ozone densities between middle and equatorial latitudes. In addition and for comparison between the kinetic model and WACCM predictions, Figure 4 includes recent nighttime global (averaged over all latitudes) atomic oxygen concentrations derived from SABER observations (solid squares) for the upper mesosphere (79–100 km) [*Smith et al.*, 2010]. Note that the atomic oxygen densities retrieved from nighttime SABER data are higher by a factor of 2 to 5 (blue shaded area) as compared to O concentrations determined from other measurements [*Russell et al.*, 2005]. The nighttime atomic oxygen measurements were derived from the Meinel band airglow emissions (detectable at a minimum altitude near 79–80 km) from vibrationally excited hydroxyl (OH) [*Smith et al.*, 2010] that limits the lowest altitude for which O densities can be estimated observationally. As seen in Figure 4, the nighttime ambient concentrations of O, O_3, and CO obtained with the present model are in reasonable agreement with the available nighttime measurements and the predictions of widely used reference models.

Once the system of equations of the time-dependent kinetic model is relaxed, that is, once the ambient concentrations of all the species become consistent with the ion pair production rate under consideration, further computations were undertaken to examine how an enhanced electron density (due to relatively weak perturbation, and due to strongly perturbed elve-related conditions) can affect the relaxation times between 76 and 92 km. In particular, an effort was made to identify the most important kinetic mechanisms acting behind the computed LORE relaxation times and how these compare with measured estimates. In this analysis, two different definitions of the LORE relaxation time (t^e_{relax} and t^{2e}_{relax}) were adopted that depend on a chosen decay factor, that is, (e or $2e$). Therefore, t^e_{relax} and t^{2e}_{relax} are the times needed for the perturbed electron density to decay by a factor e or $2e$, that is, reaching the values $n_e(t^e_{\text{relax}}) = n^0_e + \Delta n_e/e$ or $n_e(t^{2e}_{\text{relax}}) = n^0_e + \Delta n_e/2e$, where Δn_e is the perturbation of the ambient electron density (n^0_e).

In comparing with other models, *Rodger et al.* [1998] introduced the effect of an impulsive electron production mechanism under the action of background cosmic ray ionization, without further considerations on the importance of naturally occurring ambient (chemical) sources of electrons, such as associative detachment. On the other hand, the paramount importance of associative detachment reactions in the ion chemistry of the upper *D* region is generally accepted since the early 1960s [*Dalgarno*, 1961; *Whitten and Poppoff*, 1962].

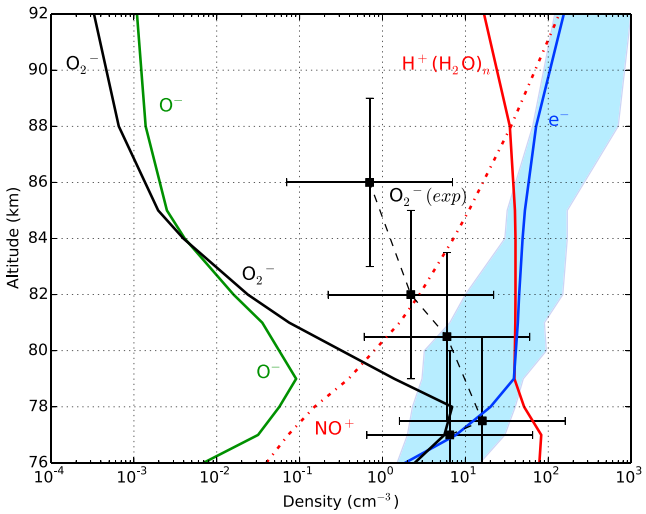

Figure 5. Ambient electron densities (solid blue line), positive ions NO^+ (dash-dotted line), positive hydrated cluster ions $H^+(H_2O)_n$ (solid red line), and negative ions (O^- and O_2^-) (solid green and black lines), according to the present kinetic model for electric discharges in air. Also plotted are available mass spectrometer measurements (squares) of nighttime *D* region O_2^- concentration reported by *Arnold and Krankowsky* [1971] and the variability (shaded blue region) of a set of nighttime *D* region electron density profiles inferred from VLF recordings and nighttime rocket experiments, presented by *Cheng et al.* [2006].

Glukhov et al. [1992] published a model using a simplified kinetic scheme including four species (electron, positive and negative ions, and positive cluster ions), accounting for electron detachment and the M-R scheme for positive cluster kinetics. The model by *Glukhov et al.* [1992] and later ones by *Pasko and Inan* [1994], *Lehtinen and Inan* [2007], and *Haldoupis et al.* [2009], which have been based on the work by *Glukhov et al.* [1992], were successfully applied to study the relaxation (over 10–100 s) of transient lower ionospheric (*D* region) disturbances caused by lightning-induced electron precipitation and directly by lightning. Thus, it is clear that both electron detachment and positive cluster kinetics should not be disregarded when studying the LORE recoveries taking place at longer time scales.

Associative detachment reactions, with rates independent of electric field, act independently of an impulsive ionization source to release free electrons by means of detachment of some negative ions through collisions with abundant ambient neutral species. In this regard, preliminary laboratory measurements by *Fehsenfeld et al.* [1967] already revealed by the late 1960s that associative detachment reactions of atmospheric interest had unexpectedly high reaction rate coefficients ($>10^{-10}$ cm^3 s^{-1}). In particular, the reactions

$$O^- + O \rightarrow O_2 + e \tag{1}$$

and

$$O_2^- + O \rightarrow O_3 + e \tag{2}$$

are of special importance in maintaining high ambient electron densities in regions of the atmosphere where the concentration of atomic oxygen is quite significant. The latter exists primarily in the upper mesosphere, above about 75 km. Note that the nighttime density of atomic oxygen naturally increases by about 6 orders of magnitude, from $\simeq$60 cm^{-3} to $\simeq 2.5 \times 10^7$ cm^{-3}, between 65 and 75 km. As shown by *Smith et al.* [2010], the nighttime atomic oxygen keeps growing above 75 km to take values up to or even higher of 10^{11} cm^{-3} at 92 km (see Figure 4). The enormous increase experienced by the ambient nighttime atomic oxygen is anticipated to have profound effects on associative detachment reactions, in which it participates.

Figure 5 shows the ambient nighttime density profiles for electrons (n_e^0) (solid blue line), positive ions NO^+ (dash-dotted line), positive cluster ions $H^+(H_2O)_n$ (solid red line), and the negative ions O^- (solid green line) and O_2^- (solid black line) resulting from the present model relaxation. Note that in Figure 5, the ambient electron density profile from 80 km to 90 km is quite flat (it hardly changes by a factor of 2). This is due to the fact that in the absence of solar radiation (nighttime conditions), the ambient ionization in the 80–90 km range is primarily due to the precipitation of high-energy particles which produce ionization that changes

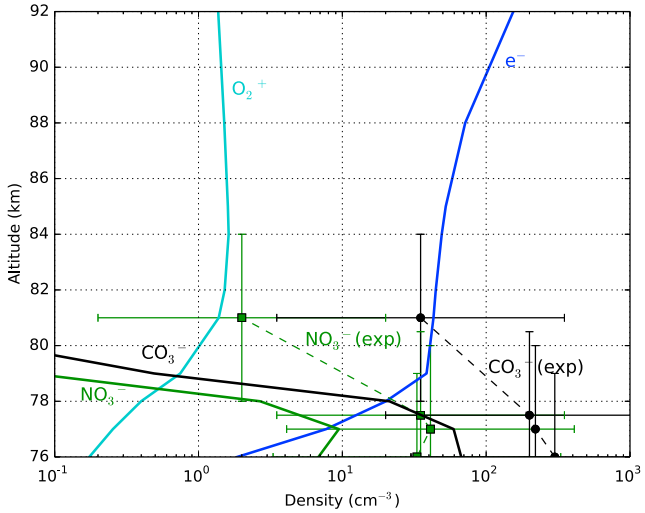

Figure 6. Computed ambient concentrations of electrons and positive ions O_2^+ (solid lines) and those of the negative ions NO_2^-, NO_3^-, and CO_2^- (solid lines). Available mass spectrometer measurements of nighttime *D* region concentrations of NO_3^- (solid squares-dashed line) and CO_3^- (solid circles-dashed line) reported by *Arnold and Krankowsky* [1971] are also shown.

only slightly, about a factor of 2, between 80 km and 90 km [*Thomas*, 1974]. The calculated trend of the nighttime NO^+ and $H^+(H_2O)_n$ densities shows that positive cluster ions disappear above about 88 km, in agreement with *Mitra* [1975]. Also shown in Figure 5 are the mass spectrometer measurements (squares) of nighttime *D* region O_2^- concentration reported by *Arnold and Krankowsky* [1971] and the range of variability (shaded blue region) of a set of nighttime *D* region electron density profiles inferred from VLF recordings and nighttime rocket measurements, published by *Cheng et al.* [2006].

Figure 6 shows the calculated ambient concentrations of electrons and positive ions O_2^+ (solid lines), along with those of the negative ions NO_2^-, NO_3^-, and CO_2^- (solid lines). Shown also in Figure 6 are the available mass spectrometer measurements of nighttime *D* region concentrations of NO_3^- (squares) and CO_3^- (circles) reported by *Arnold and Krankowsky* [1971]. Note that the measured negative ion densities shown in Figures 5 and 6 have significant uncertainties in both altitude and concentration of ~3 km and a factor of ~10, respectively [*Arnold and Krankowsky*, 1971]. In spite of these large uncertainties, the trends in the densities calculated by the kinetic model, for O_2^- (Figure 5) and NO_3^- and CO_3^- (Figure 6), are in reasonable agreement with the observations reported by *Arnold and Krankowsky* [1971].

3.1.1. Relaxation of an Electron Density Enhancement

First, the air kinetic model is applied to an increase ($\Delta n_e = 2n_e^0$) of the ambient electron density (n_e^0), for the purpose of computing the kinetic relaxation for a given, relatively weak, electron density enhancement ($n_e(t=0) = n_e^0 + \Delta n_e$), without making any assumption about the cause behind this enhancement.

A detailed analysis of the main kinetic processes underlying the relaxation of the electron density perturbation (enhancement) shows that the three-body attachment of electrons, $e + O_2 + N_2/O_2 \rightarrow O_2^- + N_2/O_2$, dominates the loss of electrons at the lower altitudes, near 76 km. As the altitude increases, however, the relative importance of two-body attachment, $e + O_3 \rightarrow O^- + O_2$, and especially that of associative detachment of O^- becomes more decisive in affecting the altitude-dependent trend of the enhanced electron density relaxation shown in Figure 7.

Figure 7 shows the time-dependent variation between 76 and 92 km of an enhanced ambient electron density ($n_e(t=0) = 3n_e^0$) in the absence of an impulsive ionization source. As seen, the relaxation time increases with altitude from 76 to 79 km, decreasing slightly between 79 km and ~81 km, remaining almost constant from 81 km to 88 km, to finally increase at higher altitudes between 88 km and 92 km. The first slight decrease in electron density after about 40 s (76 km) and 100 s (78 km and 79 km) is due to two- and three-body electron attachments producing O^- but, more importantly, O_2^- (see Figure 5). This behavior is understood by considering the characteristic times (see Figure 8) and reaction rates (see Figure 9) of the key reactions, listed in Table 4, which produce and remove electrons.

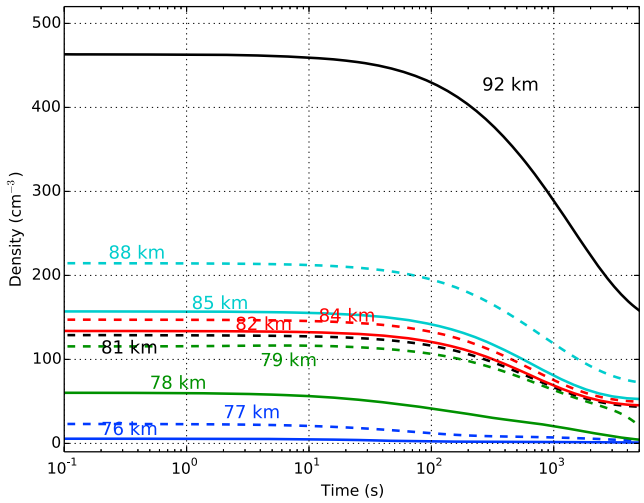

Figure 7. Time-dependent variation of the perturbed ($n_e(t=0) = 3n_e^0$) electron density between 76 and 92 km, in the absence of an impulsive ionization source.

Figure 8 shows the characteristic times (τ_i), at $t \simeq 0$ s for the fundamental kinetic processes controlling the production and loss of electrons during nighttime conditions in the *D* region. Each representative τ_i is calculated by multiplying the corresponding reaction rate coefficients k_i with the densities of the neutral reactants, e.g., $\tau_{attach}^{-1} = (k_{a1} + k_{a2})[O_3] + [O_2](k_{a3}[N_2] + k_{a4}[O_2])$ (see Table 4 for the various attachment rate coefficients). During the electron density relaxation of 5000 s, the concentrations of the neutral reactants change only slightly, by less than a factor of 2 (O_3 and O at all altitudes).

Since net charge neutrality holds, Figures 5 and 6 show that the reaction $[e] + [CO_3^-] + [NO_3^-] \simeq [H^+(H_2O)_n]$ dominates below ≃79 km, whereas the $[e] \simeq [H^+(H_2O)_n] + [NO^+] + [O_2^+]$ prevails fully above ≃79 km. Therefore, for both the electron-positive cluster and electron-positive ion dissociative recombination processes, an instant enhancement (Δn_e) in the background electron density is matched instantly in the model by the same amount in the ambient concentrations of $H^+(H_2O)_n$ at altitudes below ≃79 km. For altitudes above 79 km, the model background densities of both the positive cluster ions ($H^+(H_2O)_n$) and the dominant positive ions (NO^+ and O_2^+) match an electron density enhancement Δn_e by the weighted amounts

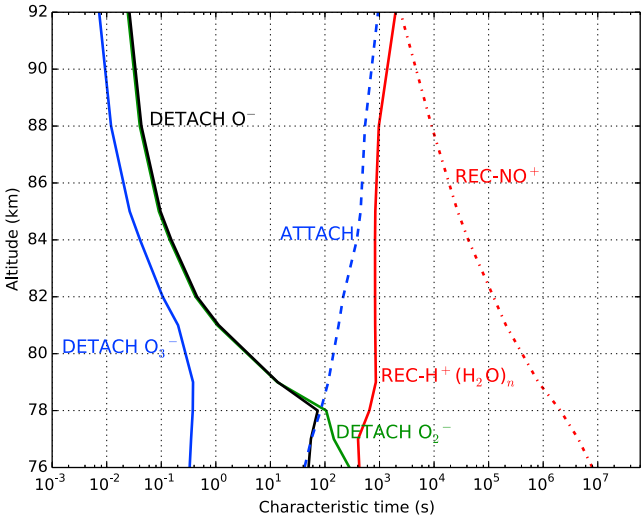

Figure 8. Detachment, attachment, and recombination characteristic times at $t \simeq 0$ s. Three different detachment characteristic times are presented, corresponding to the detachment of O^- by O, CO, O_2, and O_3 (four channels), the detachment of O_2^- by O (one channel), and the detachment of O_3^- by O and O_3 (two channels). The loss of electrons is mainly due to 3 and 2 body electron attachment (four channels, dashed line) and dissociative electron recombination with $H^+(H_2O)_n$ (solid red line) and NO^+ (two channels, dash-dotted line) producing $N(^2D)$ + O and N + O.

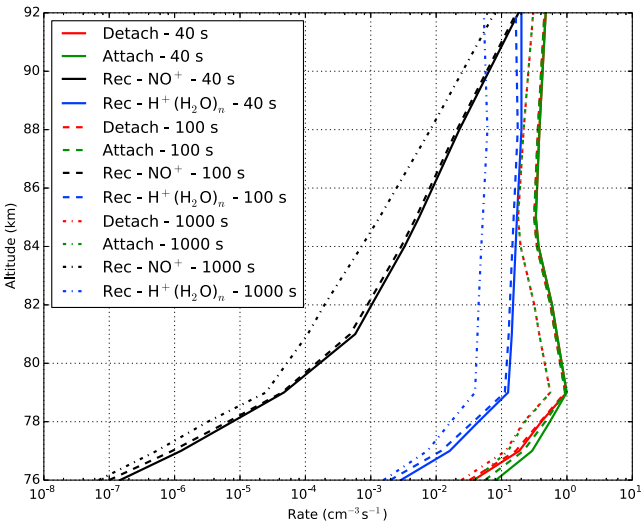

Figure 9. Different time snapshots (at 40, 100, and 1000 s) of the reactions rates of detachment (six channels, red lines), attachment (four channels, green lines), and electron recombination paths with $H^+(H_2O)_n$ (one channel, blue lines) and NO^+ (2 channels, black lines) listed in Table 4. These are calculated during the time-dependent variation of the perturbed ($n_e(t=0) = 3n_e^0$) electron density between 76 and 92 km in the absence of an impulsive ionization source.

of $\gamma_1 \Delta n_e$, $\gamma_2 \Delta n_e$, and $\gamma_3 \Delta n_e$, respectively, with $\gamma_1 + \gamma_2 + \gamma_3 \simeq 1$ and $\gamma_{1,2,3} \geq 0$. Apparently, at $t \simeq 0$ s *slightly before* the perturbation, $[H^+(H_2O)_n]^{\text{before}} = \gamma_1 n_e^0$, $[NO^+]^{\text{before}} = \gamma_2 n_e^0$, and $[O_2^+]^{\text{before}} = \gamma_3 n_e^0$, whereas at $t \simeq 0$ s *slightly after* the perturbation and above 79 km, $[H^+(H_2O)_n]^{\text{after}} = \gamma_1\, n_e^0 + \gamma_1\, \Delta n_e$, $[NO^+]^{\text{after}} = \gamma_2\, n_e^0 + \gamma_2\, \Delta n_e$, and $[O_2^+]^{\text{after}} = \gamma_3\, n_e^0 + \gamma_3\, \Delta n_e$. Figure 8 also displays approximate characteristic times at $t \simeq 0$ s for the nonlinear e-NO^+ and e-$H^+(H_2O)_n$ recombination reactions given by $\tau^{-1}_{\text{rec-NO+}} = (k_{\text{rec1}} + k_{\text{rec2}})[NO^+]^{\text{after}}$ and $\tau^{-1}_{\text{rec-H+(H2O)}n} = \alpha_d^c\, [H^+(H_2O]^{\text{after}}$.

Three different detachment relaxation times were considered in the analysis, corresponding to four O^- detachment kinetic channels (see Table 4) of O^- by O, CO, O_2, and O_3, one detachment process of O_2^- by O, and two detachment kinetic channels of O_3^- by O and O_3, respectively. As mentioned above, the loss of electrons is mainly due to three- and two-body electron attachments (four kinetic channels, see Table 4)

Table 4. Most Important Types of Detachment, Attachment, and Recombination Reactions Controlling the Concentration of Electrons[a]

Reaction	Rate Coefficient	Type
$O^- + CO \rightarrow CO_2 + e$	$k_{d1} = 6.6 \times 10^{-10}$ cm^3 s^{-1}	Detachment
$O^- + O_2 \rightarrow O_3 + e$	$k_{d2} = 5.9 \times 10^{-15}$ cm^3 s^{-1}	Detachment
$O^- + O_3 \rightarrow 2O_2 + e$	$k_{d3} = 5.3 \times 10^{-10}$ cm^3 s^{-1}	Detachment
$O^- + O \rightarrow O_2 + e$	$k_{d4} = 5.0 \times 10^{-10}$ cm^3 s^{-1}	Detachment
$O_2^- + O \rightarrow O_3 + e$	$k_{d5} = 1.5 \times 10^{-10}$ cm^3 s^{-1}	Detachment
$O_3^- + O_3 \rightarrow 3\,O_2 + e$	$k_{d6} = 1.0 \times 10^{-10}$ cm^3 s^{-1}	Detachment
$O_3^- + O \rightarrow 2\,O_2 + e$	$k_{d7} = 1.4 \times 10^{-10}$ cm^3 s^{-1}	Detachment
$e + O_3 \rightarrow O^- + O_2$	$k_{a1} \simeq 7.4 \times 10^{-12}$ cm^3 s^{-1}	Attachment
$e + O_3 \rightarrow O_2^- + O$	$k_{a2} \simeq 1.24 \times 10^{-12}$ cm^3 s^{-1}	Attachment
$e + O_2 + O_2 \rightarrow O_2^- + O_2$	$k_{a3} = 1.4 \times 10^{-29} \left(\frac{300}{T_e}\right) \exp\left(\frac{-600}{T}\right) \exp\left(\frac{700(T_e - T)}{T_e T}\right)$ cm^6 s^{-1}	Attachment
$e + O_2 + N_2 \rightarrow O_2^- + N_2$	$k_{a4} = 1.07 \times 10^{-31} \left(\frac{300}{T_e}\right)^2 \exp\left(\frac{-70}{T}\right) \exp\left(\frac{1500(T_e - T)}{T_e T}\right)$ cm^6 s^{-1}	Attachment
$e + NO^+ \rightarrow N(^2D) + O$	$k_{\text{rec1}} = 3 \times 10^{-7} \times \frac{300}{T_e}$ cm^3 s^{-1}	Recombination
$e + NO^+ \rightarrow N + O$	$k_{\text{rec2}} = 4 \times 10^{-7} \times \left(\frac{300}{T_e}\right)^{1.5}$ cm^3 s^{-1}	Recombination
$e + H^+(H_2O)_n \rightarrow$ neutrals	$\alpha_d^c = 1.0 \times 10^{-5}$ cm^3 s^{-1}	Recombination

[a]The gas (T) and electron (T_e) temperatures are both in kelvin.

electron recombination with NO^+ (two kinetic channels, see Table 4) producing $N(^2D) + O$ and $N + O$, and electron recombination with $H^+(H_2O)_n$. As shown in Figure 8, the characteristic time of the two-channel electron-ion recombination reactions (dash-dotted red line) is always higher than the characteristic times of the electron-positive charged cluster recombination (solid red line), the four-channel electron attachment reactions (dashed line), and that of the different detachment reactions (solid blue, green, and black lines). Between 76 and 78 km, the characteristic time of electron attachment is shorter (40–100 s) than that of O_2^- associative detachment (100–300 s) and, as shown in Figure 9, the electron loss is mainly controlled by the three-body attachment producing O_2^-.

At higher altitudes (79 to 92 km) detachment is much faster (see Figure 8) than attachment. However, their reactions rates become about equal at 79 km (see the snapshots shown in Figure 9); thus, electron recombination with $H^+(H_2O)_n$ and NO^+ becomes the only kinetic reaction mechanisms driving the loss of electrons between 79 and 92 km. The recombination of electrons and positive charged cluster ions dominate up to ≃88 km when electron recombination with NO^+ begins to be relatively fast. Therefore, according to the present kinetic analysis, there is a lower region (76 to 79 km) where LORE relaxation times are controlled by a three-body attachment process producing O_2^-. Next, there is a higher region above 79 km where the relative efficiencies of attachment and associative detachment are the same, and thus, LORE relaxation times are driven by the time scale of electron-$H^+(H_2O)_n$ recombination. Finally, above 88 km, and because of the growing density of NO^+ (see Figures 5 and 9), the recombination time of electrons with NO^+ is sufficiently fast so that electrons take the longest time to relax to ambient values by means of recombining with NO^+. This suggests the possibility that long-lasting (>10 min and up to 30 min) LORE events can take place between 79 km and 88 km, although it is unlikely that VLF could penetrate beyond 85 km. Note that according to observations (see Figure 3), most LORE recovery times are shorter than 15 min. Between 79 km and 88 km, the recombination reaction rate of electron-positive clusters remains almost constant in altitude, whereas the electron-NO^+ recombination increases (see Figure 9), leading to stable, or slightly longer, LORE relaxation times.

3.1.2. A Perturbation Caused by a Large EMP Field

Here the same kinetic model is used to investigate the dynamics of a LORE-related electron density perturbation, which is produced by lightning EMP electron impact in the upper *D* region. To pursue this case, the finite difference time domain (FDTD) code GREMPY, developed by *Luque et al.* [2014], was applied to model the effects on the upper *D* region of an intense lightning return stroke with a peak current of 400 kA and characteristic rise and decay times $\tau_r = 20$ μs and $\tau_f = 50$ μs, respectively. Within the lifetime of the EMP field, the only effects on the plasma medium are governed by the processes of impact ionization and electron dissociative attachment. The dynamics of the reduced electric field at *D* region heights, which results from the lightning EMP under consideration, are illustrated in Figure 10 as a function of time and altitude. By inserting the *D* region reduced fields into the full chemical code, the dynamics of the elevated electron density were computed and investigated during both the impulsive action of the EMP field and the much slower electron relaxation phase. The main findings are presented below in brief.

The perturbed electron densities in the altitude range between 76 and 92 km are plotted as a function of time for several altitudes in Figure 11. This range of altitudes was chosen in order to include all uppermost *D* region heights that could be reached by VLF waves propagating in the Earth-ionosphere waveguide during nighttime. As seen, there is first a sharp increase of the electron density between 0.40 ms and 0.45 ms in response to the rise and the maximum of the reduced EMP electric field, which was depicted in Figure 10. Right after the first electron density enhancement, there is a second weak augmentation of the electron density around 0.50 ms caused by the impact of a second peak in the EMP electric field occurring between 0.5 ms (at 76 km) and 0.53 ms (at 92 km), as seen in Figure 10. Once the EMP field is gone, after about 2.5 ms, the electron density relaxation phase begins. What is seen first during this regime is a hump in electron density which starts near 10 ms. This is attributed to the action of associative detachment that releases electrons from negatively charged ions (mainly O^- and O_2^-), whose concentrations have been previously enhanced by the action of the lightning EMP. This secondary increase that last for about 10 s is followed by a relaxation in electron density which is strongly dependent on altitude. As seen in Figure 11, the longest relaxation time occurs at 88 km and 92 km, which is attributed to the combined action of electron recombination with $H^+(H_2O)_n$ (at 88 km and below) and NO^+ (at 92 km) ions.

The altitude dependence of electron density relaxation times, insinuated in Figures 7 and 11, is summarized in a conceivable way in Figure 12, for the altitude range between 76 and 92 km, for both scenario cases considered in the present study. Shown there with green solid (t^e_{relax}) and dashed (t^{2e}_{relax}) lines are the electron density

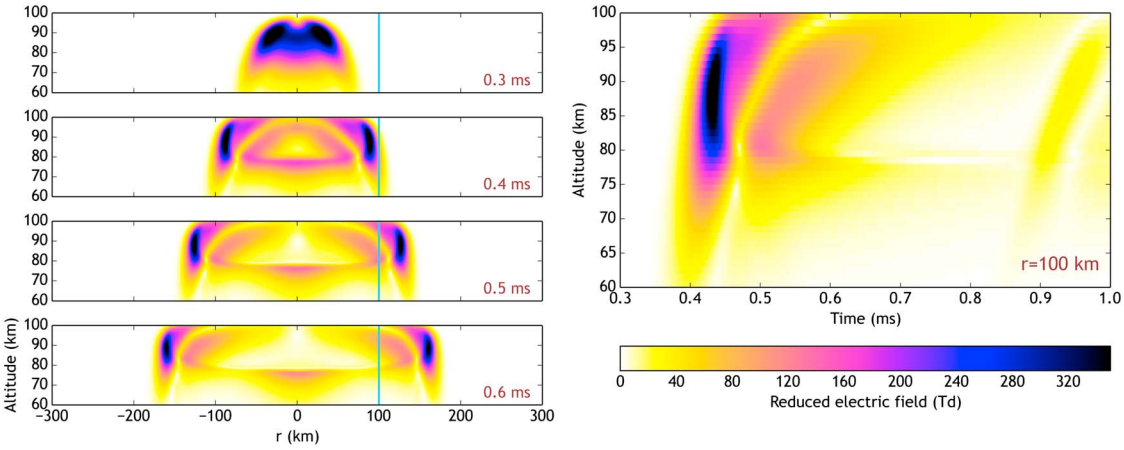

Figure 10. Upper altitude reduced electric fields associated to a lightning EMP causing an ELVE and ionization in the upper mesosphere. The calculations were made with a finite differences time domain (FDTD) code. The EMP shown is associated to an intense lightning return stroke with a peak current of 400 kA. (left) Four snapshots of the reduced electric field distribution as a function of altitude and radial distance *r*, from the causative CG lightning. (right) The time evolution of the reduced electric fields along an altitude range from 60 to 100 km, taken at 100 km away from the parent lightning position, as shown by the blue line in Figure 10 (left).

relaxation times simulated for a weaker perturbation in the absence of an electric field, whereas the blue solid (t^{e}_{relax}) and dashed (t^{2e}_{relax}) lines represent the relaxation times associated with the case of an EMP-driven ionization source that is capable of causing a LORE due to much larger elevation in electron density. As expected, the LORE relaxation times become longer when larger decay factors, 2*e*, rather than smaller, *e*, are considered. It is worth mentioning that the relaxation times for heights below 78 km become short, that is, less than ≃80 s. Such times are comparable with the recoveries of typical early VLF events, which are known to be often associated with sprites that appear to be located mostly below ~80 km [e.g., see *Inan et al.*, 2010]. One, however, should be cautious in generalizing this implication, because sprites, as well as sprite halos, are also known to extend at times above 80 km.

Finally, it is also noticeable in Figure 12 that below ~79 km, the electron relaxation times are almost the same for both the EMP and non-EMP cases, because the driving electron loss mechanism, that is, electron attachment has a linear dependence on electron density, n_e. On the other hand, for heights greater than ~79 km, electron loss is dominated by the mechanisms of dissociative recombination of electrons with $H^+(H_2O)_n$ (mostly between 79 km and 88 km) and NO^+ (mostly above 88 km), when it prevails a nonlinear (quadratic) dependence on electron density. In addition, one should note that below ≃85 km, the modeled electron

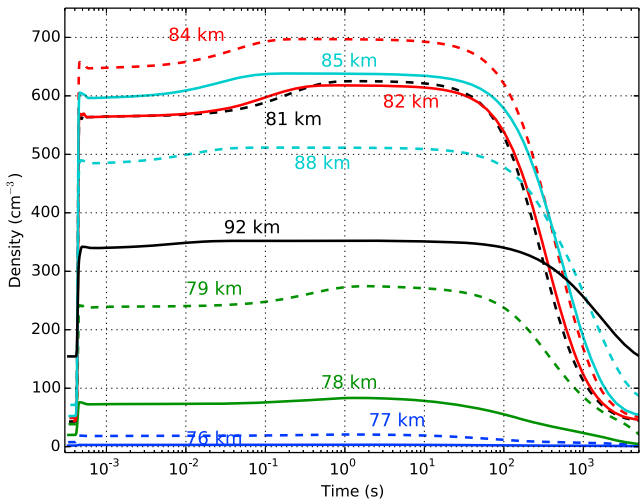

Figure 11. Time-dependent evolution of electron density enhancements at altitudes between 76 and 92 km caused by an impulsive source of ionization driven by the lightning-induced EMP shown in Figure 10.

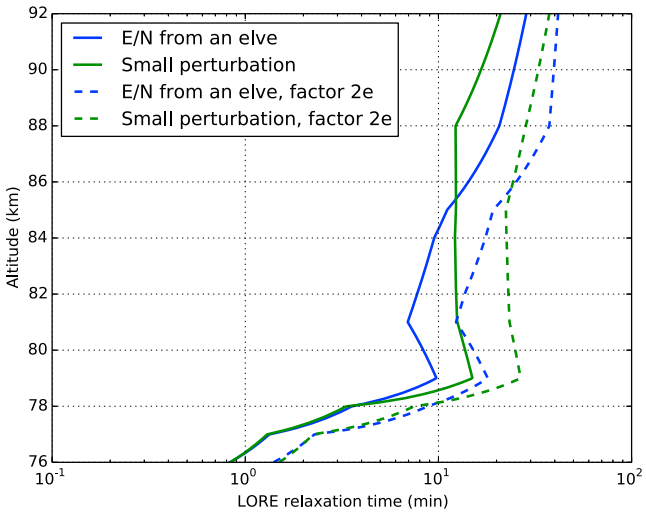

Figure 12. Computed electron density relaxation times t^{e}_{relax} (solid lines) and t^{2e}_{relax} (dashed lines) between 76 and 92 km for the cases of a perturbed initial electron density ($n_e(t=0) = 3n^0_e$) that is unrelated to an impulsive ionization source (solid green line) and for the case of an impulsive ionization source (solid blue line) associated with a lightning-induced electromagnetic pulse (EMP) which impacts in the upper *D* region causing elve emissions and LORE-related elevations in electron density. Two different definitions of the LORE relaxation time (t^{e}_{relax} and t^{2e}_{relax}) are shown to depend on the chosen decay factor (*e* or 2*e*). Longer LORE relaxation times are obtained when a larger decay factor is used, that is, 2*e* rather than *e*.

density enhancement *is smaller for* the non-EMP case than it is in the EMP case. All this causes the relaxation times below ≃85 km to become shorter in the EMP case, as compared to the non-EMP case, simply because recombination depends on the square of electron density. As for altitudes above ≃85 km, when n_e reaches its maximum value in the non-EMP case, the concentration of $H^+(H_2O)_n$ is smaller in the EMP case, than in the non-EMP one, resulting in longer relaxation times. It is worth mentioning that the difference in the non-EMP and EMP positively charged cluster concentration is due to (1) the difference in ion pair production assumed in the non-EMP (see section 3.1.1) and (2) calculated in the EMP case.

3.2. Time Scale Analysis

In order to understand better the mechanisms behind the LORE long recoveries, it is useful to strip the full kinetic model to its essential reactions. The analyses in the previous sections show that the evolution of the electron density is determined by attachment, detachment, and recombination processes. The main attachment and detachment reactions are

$$e + O_3 \xrightarrow{k_{a1}} O^- + O_2, \tag{3}$$

$$e + O_2 + O_2 \xrightarrow{k_{a3}} O_2^- + O_2, \tag{4}$$

$$e + O_2 + N_2 \xrightarrow{k_{a4}} O_2^- + N_2, \tag{5}$$

$$O^- + O_2 \xrightarrow{k_{d2}} e + O_3, \tag{6}$$

$$O^- + O \xrightarrow{k_{d4}} e + O_2, \tag{7}$$

$$O_2^- + O \xrightarrow{k_{d5}} e + O_3, \tag{8}$$

$$O_2^- + O \xrightarrow{k_{ex}} O^- + O_2. \tag{9}$$

Other negative ion conversion reactions (apart from reaction (9)) converting O_2^- to O_3^- and O_4^- play a minor role. The reaction converting O_2^- to O_3^- has a rate coefficient similar to that of (9), but the ambient concentration of O is between 1 and 3 orders of magnitude higher than the ambient density of O_3 in the altitude

range considered (see Figure 4). Moreover, the conversion of O_2^- to O_4^- mainly occurs through three-body processes, which are not very efficient at mesospheric altitudes. Thus, although the full kinetic model includes many different negative ion conversion reactions, the simplified kinetic scheme in this section only considers the dominant negative ion conversion producing O^- from O_2^-.

Electrons recombine with positive molecular and cluster ions. The dominant molecular positive ion is NO^+, which recombines with electrons in the reaction

$$e + NO^+ \xrightarrow{\alpha_d^m} N + O. \tag{10}$$

The recombination of electrons with clusters $H^+(H_2O)_n$, which is significantly faster than molecular recombination, proceeds with the reaction

$$e + H^+(H_2O)_n \xrightarrow{\alpha_d^c} \text{Neutrals}. \tag{11}$$

As detailed above, the cluster ions are considered, in line with [*Mitra and Rowe*, 1972], to be created by the conversion of molecular positive ions at a rate $B = N^2 10^{-31}$ cm^6 s^{-1}, where N is the total density of neutrals.

Finally, this simplified model is completed by a source of ionization that creates pairs of oppositely charged particles at a given rate g. Most of the rate coefficients of the reactions (3)–(9) and (10) and (11) are listed in Table 4; in addition, $k_{ex} = 3.310 \times 10^{-10}$ cm^{-3} s^{-1} and $\alpha_d^m = k_{\text{rec1}} + k_{\text{rec2}}$.

This simplified chemical reaction system can be divided into two subsystems. The first one, which is called attachment-detachment subsystem, comprises reactions (3)–(9) and accounts for the transfer of negative charges. The second subsystem, which is named here recombination subsystem, involves the recombination reactions (10) and (11) as well as the conversion of positive ions and the creation of new charge pairs. The typical time scales of the two subsystems can be determined by treating them separately. This is justifiable because of the wide separation that is anticipated between these two time scales.

3.2.1. Attachment-Detachment Balance

Neglecting variations in the densities of neutral species in (3)–(9), the evolution of negatively charged species is determined by the following set of equations:

$$\frac{\mathrm{d}}{\mathrm{d}t}\begin{pmatrix} n_e \\ n_1 \\ n_2 \end{pmatrix} = A \begin{pmatrix} n_e \\ n_1 \\ n_2 \end{pmatrix} + \begin{pmatrix} g - S_{\text{rec}} \\ 0 \\ 0 \end{pmatrix}, \tag{12}$$

where

$$A = \begin{pmatrix} -\nu_{a3} - \nu_{a4} - \nu_{a1} & \nu_{d2} + \nu_{d2} & \nu_{d5} \\ \nu_{a1} & -\nu_{d2} - \nu_{d4} & \nu_{ex} \\ \nu_{a3} + \nu_{a4} & 0 & -\nu_{d5} - \nu_{ex} \end{pmatrix}. \tag{13}$$

In the above equations, n_e is the electron density, n_1 and n_2 are the densities of O^- and O_2^-, respectively, while S_{rec} accounts for the removal of electrons through recombination processes. Each ν_i is obtained from k_i in (3)–(9) by multiplying with the immutable densities of the neutral reactants, e.g., $\nu_{a3} = k_{a3}[O_2]^2$, so that through this dependence all ν_i depend on altitude.

Note that the matrix A is singular, and therefore, one of its eigenvalues is zero. This is a consequence of the conservation of charge by the system of reactions (3)–(9):

$$\frac{\mathrm{d}}{\mathrm{d}t}(n_e + n_1 + n_2) = 0. \tag{14}$$

The eigenvectors (n_e, n_1, n_2) with eigenvalue zero cover a continuous family of quasi-equilibrium states which is written as $(n_e, n_1, n_2) = m(r_e, r_1, r_2)$, where $r_e + r_1 + r_2 = 1$ and $m = (n_e + n_1 + n_2)$. The values of the r_i, plotted in Figure 13a, describe the relative equilibrium densities of each of the above three species. Figure 13b shows the relaxation times of the linear system at each altitude, defined as the inverse of the two nonzero eigenvalues of A. These values define the time scale of the attachment-detachment subsystem, which lies between several seconds and some minutes.

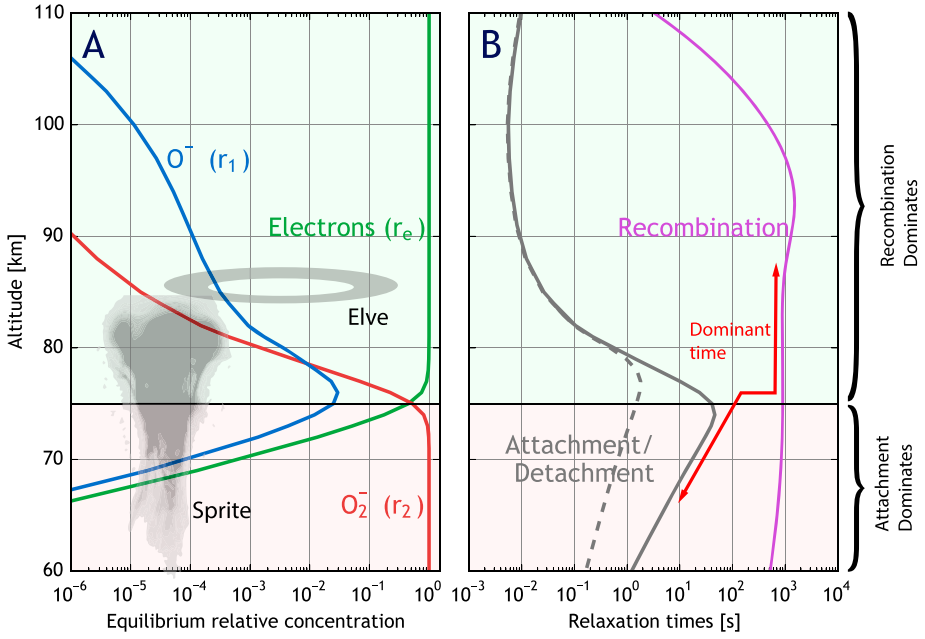

Figure 13. (a) Quasi-equilibrium relative concentrations of the three dominant negatively charged species. (b) Relaxation times of the attachment/detachment subsystem (gray) and linear relaxation time of recombination with NO^+. The shaded TLE structures in Figure 13 are provided to approximately indicate the altitude range of sprites and elves. The red line in Figure 13 indicates the dominant time scale on which the electron density relaxes. As seen, there is a sharp jump at a transition altitude near 75 km; above this altitude the attachment/detachment subsystem cancels itself; therefore, electron loss at higher altitudes is dominated by the much slower recombination relaxation rates.

Figure 13 exhibits two differentiated regimes: (1) One below 75 km where all negative charges are converted into O_2^- in a time scale that varies from about 1 s at 60 km to about 1 min at 75 km. In this regime an electron density elevation is quickly depleted by being converted into an equal population of the much less mobile O_2^-. Thus, it does possibly reconcile with the short relaxation time of early fast events. (2) Above 75 km free electrons dominate by far the negative charges in an attachment-detachment quasi-equilibrium situation, so that, although the relaxation times governed by attachment are short, the conductivity does not relax within these short time scales. This is the regime of long recovery times that characterize the long-living LORE perturbations.

3.2.2. Recombination and Decay Toward Equilibrium

The arguments in the previous sections explain the long recovery times of atmospheric conductivity above 75 km. However, to obtain a quantitative prediction, which could be compared with the observations, one needs to investigate the characteristic times of the recombination reactions (10) and (11). Since these times are anticipated to be considerably longer than the characteristic times of the attachment-detachment subsystem investigated in the previous section, it is reasonable to assume from there on that the attachment-detachment reactions are fully relaxed (i.e., $A(n_e, n_1, n_2)^T = 0$ in the notation of equation (12)). Under these conditions, and because free electrons at higher altitudes dominate the negative charges, the electron density equals the sum of the cluster and molecular ions,

$$n_e = n_m + n_c, \tag{15}$$

where $n_m = [NO^+]$ and $n_c = [H^+(H_2O)_n]$ are the number densities of molecular and cluster ions, respectively.

The evolution of these densities obeys the following set of differential equations:

$$\frac{dn_e}{dt} = -\alpha_d^m n_e n_m - \alpha_d^c n_e n_c + g, \tag{16}$$

$$\frac{dn_m}{dt} = -\alpha_d^m n_e n_m + g - B n_m, \tag{17}$$

$$\frac{dn_c}{dt} = -\alpha_d^c n_e n_c + B n_m. \tag{18}$$

By using (15), it turns out that the equilibrium electron density of this system of equations, n_{e0}, satisfies the condition:

$$\frac{\alpha_d^c n_{e0}^2 \left(B + \alpha_d^m n_{e0}\right)}{B + \alpha_d^c n_{e0}} = g. \tag{19}$$

In this equilibrium, the ratio between the density of clusters and the total density of positively charged species, $x = n_c/n_e = n_c/(n_c + n_m)$, is given by

$$x_0 = \frac{B}{B + \alpha_d^c n_{e0}}. \tag{20}$$

Next, in order to obtain a relaxation time scale, one needs to rewrite equation (16) as

$$\frac{\mathrm{d}n_e}{\mathrm{d}t} = -n_e^2 \bar{\alpha} + g, \tag{21}$$

with an effective recombination coefficient $\bar{\alpha} = (1 - x)\alpha_d^m + x\alpha_d^c$. If, for simplicity, it is assumed that x takes always its equilibrium value from (20), equation (21) can be linearized close to equilibrium ($n_e(t) = n_{e0} + \delta n_e(t)$, $\delta n_e(t) \ll n_{e0}$) to derive a relaxation time $\tau = 1/(2\sqrt{\bar{\alpha} g})$. By using the production rate g from *Thomas* [1974], and solving for n_{e0} in (19), one finds the recombination times plotted in Figure 13. As a consistency check, it is noted that the recombination time scale is everywhere significantly longer than the attachment-detachment time scales; thus, the adopted approach of treating these two subsystems separately is justified.

Figure 13 provides an illustrative summary of the different relaxation times observed in VLF perturbations. Sprites, which occur in a range of altitudes from about 65 km to 85 km, create electron density enhancements, which are detectable by VLF waves at lower altitudes, possibly below ≃80 km. As shown, an electron enhancement located at these heights relaxes at time scales of many seconds to several tens of seconds, that is, in general agreement with the observed recoveries of typical early/fast VLF events, which are known to associate with sprite discharges.

On the other hand, LOREs associate with elves which are located above 80 km where the relaxation of electron density enhancements is taking much longer, having characteristic times of several to many minutes.

In this frame of interpretation, the transition altitude which is identified here to be at about 75 km is somewhat smaller but, in general, compares well with the altitude obtained with the full kinetic model (79 km). One should note, however, that the exact transition altitude depends on the presumed concentrations of O and O_3, used as model inputs. Since these concentrations are highly variable in the upper mesosphere, one may expect some variation in the transition altitude between the regimes of attachment- and recombination-dominated electron density relaxation.

4. Summary and Concluding Comments

The principal findings of this paper are summarized as follows:

1. Using a full kinetic model, the upper mesosphere kinetic reaction mechanisms, including those which control the kinetics of hydrated positive cluster ions, were investigated and applied to the case of lightning EMP electron density production in the nighttime *D* region ionosphere.
2. Two possible scenarios were investigated: (a) the relaxation of a small enhancement in ambient electron density without having to invoke an impulsive ionization source for its production and (b) the relaxation of a much stronger (factor of ≃20 above ambient values) electron density enhancement caused by the impact in the upper *D* region plasma of impulsive EMP fields induced by a very intense +CG lightning discharge of ∼400 kA, that is, an EMP field which is expected to produce LOREs and elves. The full nonequilibrium kinetic modeling of the perturbation dynamics in the 76 to 92 km altitude range showed that electron density relaxation times are controlled by attachment at lower altitudes, from about 75 to 78 km, while above ∼80 km attachment is fully canceled by associate detachment of negative ions (mainly O^- and O_2^-) with ground neutrals of significant mesospheric number densities, as is atomic oxygen at night. In this way the loss of electrons at anticipated LORE (and elve) altitudes (>80 km) is overwhelmingly controlled by dissociative recombination reactions, mostly of electrons with $H^+(H_2O)_n$ ions and secondarily with NO^+ ions, with the latter to dominate the process above about 88 km.

3. Important associative detachment reactions in the upper mesosphere, particularly those of high rates ($>10^{-10}$ cm^3 s^{-1}) act to produce free electrons regardless of the presence or not of an impulsive ionization source driven by an electromagnetic pulsed electric field and/or possibly also a quasi-electrostatic (QE) field source.
4. A separate time scale analysis of the relaxation of mesospheric *D* region electron density perturbations, was introduced and applied successfully for the purpose of gaining a better physical insight and for testing the findings of the complicated, but more accurate, full kinetic model. The agreement between the two models is fairly good. In general terms, both models show that (a) short electron density relaxation times prevail below about 80 km and compare well with the observed lifetimes of typical early/fast events, which are known to associate with sprites, and (b) electron density elevations live much longer above about 80 km where lightning-induced intense EMPs impact on the upper *D* region to generate long-living, large electron density disturbances which are responsible for LORE type VLF perturbations and also for producing elves.
5. The full nonequilibrium kinetic model simulations indicate that the long electron density relaxation times occur above about 79 km, where electron loss by attachment is canceled by the action due to detachment; thus, lifetime of electrons is determined at these heights by recombination with $H^+(H_2O)_n$ and NO^+.

The results of the present study helped quantify and understand the lightning EMP effects on electron density production and relaxation in the nighttime upper *D* region. In general, the simulation results on electron density relaxation times are consistent with observations of LORE recovery times [*Haldoupis et al.*, 2012, 2013].

It should be stressed that although the present chemical models were applied for the case of strong lightning-induced EMP effects on the upper *D* region, they also qualify for a source of ionization production that relates with lightning-generated quasi-electrostatic (QE) fields in the upper atmosphere, that is, fields which are known to generate momentary sprite discharges and halo displays. This implies that the models used here may also be accountable for long-living early-type VLF events which may occur in association with high altitude (>80 km) sprite discharges, sprite halos, and even the highest part of gigantic jets. Although there is not yet any VLF evidence suggesting it is happening, this option needs to be kept in mind and investigated in future studies.

Finally, it needs to be pointed out that this paper does not model VLF scattering from the long-lived, electron density inhomogeneities that produce the LORE perturbations. This type of quantitative analysis is important for the ultimate validation of the present chemical model. However, it constitutes a major task which was set outside the scope of this work but needs to be undertaken in one or more future studies.

Acknowledgments

We thank Morris Cohen and Umran Inan for their continuous support with the VLF data and Stefano Dietrich for providing Italian LINNET data. This work was supported by the Spanish Ministry of Science and Innovation, MINECO under projects ESP2013-48032-C5-5-R, FIS2014-61774-EXP, and ESP2015-69909-C5-2-R, and by the EU through the FEDER program. A.L. acknowledges support by a Ramón y Cajal contract, code RYC-2011-07801. C.H. acknowledges the support received from the European Science Foundation (ESF) for a short visit to Granada (Spain), within the ESF network entitled "Thunderstorm effects on the atmosphere-ionosphere system (TEA-IS)." All data used in this paper are directly available after a request is made to authors F.J.G.V. (vazquez@iaa.es), A.L. (aluque@iaa.es), or C.H. (chald@physics.uoc.gr).

References

Arnold, F., and D. Krankowsky (1971), Negative ions in the lower ionosphere: A comparison of a model computation and a mass-spectrometric measurement, *J. Atm. Sol. Terr. Phys.*, *33*, 1693–1702.

Barrington-Leigh, C. P., and U. S. Inan (1999), Elves triggered by positive and negative lightning discharges, *Geophys. Res. Lett.*, *26*, 683–686, doi:10.1029/1999GL900059.

Betz, H. D., K. Schmidt, P. Oestinger, and M. Wirz (2004), Lightning detection with 3-D discrimination of intracloud and cloud-to-ground discharges, *Geophys. Res. Lett.*, *31*, L11108, doi:10.1029/2004GL019821.

Blaes, P. R., R. A. Marshall, and U. S. Inan (2016), Global occurrence rate of elves and ionospheric heating due to cloud-to-ground lightning, *J. Geophys. Res. Space Physics*, *121*, 699–712, doi:10.1002/2015JA021916.

Brasseur, G. P., and S. Solomon (1986), *Aeronomy of the Middle Atmosphere*, 2nd ed., Reidel, Boston, Mass.

Capitelli, M., C. M. Ferreira, and B. F. Gordiets (2000), *Plasma Kinetics in Atmospheric Gases, Atomic, Optical and Plasma Physics*, Osipov, A. I., Springer, Berlin.

Chen, A. B., et al. (2008), Global distributions and occurrence rates of transient luminous events, *J. Geophys. Res.*, *113*, A08306, doi:10.1029/2008JA013101.

Cheng, Z., S. A. Cummer, D. N.-T. Baker, and S.-G. Kanekal (2006), Nighttime D region electron density profiles and variabilities inferred from broadband measurements using VLF radio emissions from lightning, *J. Geophys. Res.*, *111*, A05302, doi:10.1029/2005JA011308.

Cohen, M. B., U. S. Inan, and E. W. Paschal (2010), Sensitive broadband ELF/VLF radio reception with the AWESOME instrument, *IEEE Trans. Geosci. Remote Sens.*, *48*(1), 3–16, doi:10.1109/TGRS.2009.2028331.

Cotts, B. R., and U. S. Inan (2007), VLF observation of long ionospheric recovery events, *Geophys. Res. Lett.*, *34*, L14809, doi:10.1029/2007GL030094.

Dalgarno, A. (1961), Charged particles in the upper atmosphere, *Ann. Geophys.*, *17*(1), 16–49.

Fehsenfeld, F. C., A. L. Schmeltekopf, H. I. Schiff, and E. E. Ferguson (1967), Laboratory measurements of negative ion reactions of atmospheric interest, *Planet. Space Sci.*, *15*, 373–379.

Glukhov, V. S., V. P. Pasko, and U. S. Inan (1992), Relaxation of transient lower ionospheric disturbances caused by lightning-whistler-induced electron precipitation bursts,*J. Geophys. Res.*, *97*, 16,971–16,979, doi:10.1029/92JA01596.

Gordillo-Vázquez, F. J. (2008), Air plasma kinetics under the influence of sprites, *J. Phys. D*, *41*, 234016, doi:10.1088/0022-3727/41/23/234016.

Gordillo-Vázquez, F. J. (2010), Vibrational kinetics of air plasmas induced by sprites, *J. Geophys. Res.*, *115*, A00E25, doi:10.1029/2009JA014688.
Gordillo-Vázquez, F. J., and A. Luque (2010), Electrical conductivity in sprite streamer channels, *Geophys. Res. Lett.*, *37*, L16809, doi:10.1029/2010GL044349.
Gordillo-Vázquez, F. J., A. Luque, and M. Simek (2011), Spectrum of sprite halos, *J. Geophys. Res.*, *116*, A09319, doi:10.1029/2011JA016652.
Gordillo-Vázquez, F. J., A. Luque, and M. Simek (2012), Near infrared and ultraviolet spectra of TLEs, *J. Geophys. Res.*, *117*, A05329, doi:10.1029/2012JA017516.
Haldoupis, C., T. Neubert, U. S. Inan, A. Mika, T. H. Allin, and R. A. Marshall (2004), Subionospheric early VLF signal perturbations observed in one-to-one association with sprites, *J. Geophys. Res.*, *109*, A10303, doi:10.1029/2004JA010651.
Haldoupis, C., Á. Mika, and S. Shalimov (2009), Modeling the relaxation of early VLF perturbations associated with transient luminous events, *J. Geophys. Res.*, *114*, A00E04, doi:10.1029/2009JA014313.
Haldoupis, C., N. Amvrosiadi, B. R. T. Cotts, O. A. van der Velde, O. Chanrion, and T. Neubert (2010), More evidence for a one-to-one correlation between Sprites and Early VLF perturbations, *J. Geophys. Res.*, *115*, A07304, doi:10.1029/2009JA015165.
Haldoupis, C., M. Cohen, B. R. Cotts, E. Arnone, and U. Inan (2012), Long lasting D-region ionospheric modifications, caused by intense lightning in association with elve and sprite pairs, *Geophys. Res. Lett.*, *39*, L16801, doi:10.1029/2012GL052765.
Haldoupis, C., M. Cohen, E. Arnone, B. R. Cotts, and S. Dietrich (2013), Step-like and long-recovery VLF perturbations caused by EM pulses radiated by powerful ± CG lightning discharges, *J. Geophys. Res. Space Physics*, *118*, 5392–5402, doi:10.1002/jgra.50489.
Inan, U. S., V. P. Pasko, and T. F. Bell (1996), Sustained heating of the ionosphere above thunderstorms as evidenced in "early/fast" VLF events, *Geophys. Res. Lett.*, *23*, 1067–1070, doi:10.1029/96GL01360.
Inan, U. S., S. A. Cummer, and R. A. Marshall (2010), A survey of ELF and VLF research on lightning-ionosphere interactions and causative discharges, *J. Geophys. Res.*, *115*, A00E36, doi:10.1029/2009JA014775.
Kaufmann, M., O. A. Gusev, K. U. Grossmann, F. J. Martin-Torres, D. R. Marsh, and A. A. Kutepov (2003), Satellite observations of daytime and nighttime ozone in the mesosphere and lower thermosphere, *J. Geophys. Res.*, *108*(9), 4272, doi:10.1029/2002JD002800.
Kossyi, I. A., A. Y. Kostinsky, A. A. Matveyev, and V. P. Silakov (1992), Kinetic scheme of the non-equilibrium discharge in nitrogen-oxygen mixtures, *Plasma Sources Sci. Technol.*, *1*, 207–220, doi:10.1088/0963-0252/1/3/011.
Lehtinen, N. G., and U. S. Inan (2007), Possible persistent ionization caused by giant blue jets, *Geophys. Res. Lett.*, *34*, L08804, doi:10.1029/2006GL029051.
Luque, A., and F. J. Gordillo-Vázquez (2011), Mesospheric electric breakdown and delayed sprite ignition caused by electron detachment, *Nat. Geosci.*, *5*, 22–25, doi:10.1038/ngeo1314.
Luque, A., D. Dubrovin, F. J. Gordillo-Vázquez, U. Ebert, F. C. Parra-Rojas, Y. Yair, and C. Price (2014), Coupling between atmospheric layers in gaseous giant planets due to lightning-generated electromagnetic pulses, *J. Geophys. Res. Space Physics*, *119*, 8705–8720, doi:10.1002/2014JA020457.
Marsh, D. R., M. J. Mills, D. E. Kinnison, J. F. Lamarque, N. Calvo, and L. M. Polvani (2013), Climate change from 1850 to 2005 simulated in CESM1 (WACCM), *J. Clim.*, *26*(19), 7372–7391, doi:10.1175/JCLI-D-12-00558.1.
Marshall, R. A. (2012), An improved model of the lightning electromagnetic field interaction with the D-region ionosphere, *J. Geophys. Res.*, *117*, A03316, doi:10.1029/2011JA017408.
Marshall, R. A., U. S. Inan, and W. A. Lyons (2006), On the association of early/fast very low frequency perturbations with sprites and rare examples of VLF backscatter, *J. Geophys. Res.*, *111*, D19108, doi:10.1029/2006JD007219.
Mitra, A. P. (1975), *D*-region in disturbed conditions, including flares and energetic particles, *J. Atmos. Sol. Terr. Phys.*, *37*, 895–913.
Mitra, A. P., and J. N. Rowe (1972), Ionospheric effects of solar flares—VI. Changes in *D*-region ion chemistry during solar flares, *J. Atmos. Sol. Terr. Phys.*, *34*, 795–806.
Neubert, T., et al. (2005), Co-ordinated observations of transient luminous events during the EuroSprite2003 campaign, *J. Atmos. Sol. Terr. Phys.*, *67*, 807–820, doi:10.1016/j.jastp.2005.02.004.
Newsome, R. T., and U. S. Inan (2010), Free-running ground-based photometric array imaging of transient luminous events, *J. Geophys. Res.*, *115*, A00E41, doi:10.1029/2009JA014834.
Parra-Rojas, F. C., A. Luque, and F. J. Gordillo-Vázquez (2013), Chemical and electrical impact of lightning on the Earth mesosphere: The case of sprite halos, *J. Geophys. Res. Space Physics*, *118*, 5190–5214, doi:10.1002/jgra.50449.
Parra-Rojas, F. C., A. Luque, and F. J. Gordillo-Vázquez (2015), Chemical and thermal impact of sprite streamers in the Earth mesosphere, *J. Geophys. Res. Space Physics*, *120*, 8899–8933, doi:10.1002/2014JA020933.
Pasko, V. P. (2010), Recent advances in theory of transient luminous events, *J. Geophys. Res.*, *115*, A00E35, doi:10.1029/2009JA014860.
Pasko, V. P., and U. S. Inan (1994), Recovery signatures of lightning-associated VLF perturbations as a measure of the lower ionosphere, *J. Geophys. Res.*, *99*, 17,523–17,538, doi:10.1029/94JA01378.
Pasko, V. P., Y. Yair, and C.-L. Kuo (2012), Lightning related transient luminous events at high altitude in the Earth's atmosphere: Phenomenology, mechanisms and effects, *Space Sci. Rev.*, *168*, 475–516, doi:10.1007/s11214-011-9813-9.
Rakov, V. A., and M. A. Uman (2003), *Lightning Physics and Effects*, Cambridge Univ. Press, Cambridge, U. K.
Rodger, C. J. (2003), Subionospheric VLF perturbations associated with lightning discharges, *J. Atmos. Sol. Terr. Phys.*, *65*, 591–606.
Rodger, C. J., O. A. Molchanov, and N. R. Thomson (1998), Relaxation of transient ionization in the lower ionosphere, *J. Geophys. Res.*, *103*, 6969–6975, doi:10.1029/98JA00016.
Russell, J. P., W. E. Ward, R. P. Lowe, G. Roble, G. G. Sheperd, and B. Solheim (2005), Atomic oxygen profiles (80 to 115 km) derived from Wind Imaging Interferometer/Upper Atmospheric Research Satellite measurements of the hydroxyl and greenline airglow: Local time latitude dependence, *J. Geophys. Res.*, *110*, D15305, doi:10.1029/2004JD005570.
Salut, M. M., M. Abdullah, K. L. Graf, M. B. Cohen, B. R. Cotts, and S. Kumar (2012), Long recovery VLF perturbations associated with lightning discharges, *J. Geophys. Res.*, *117*, A08311, doi:10.1029/2012JA017567.
Salut, M. M., M. B. Cohen, M. A. M. Ali, K. L. Graf, B. R. Cotts, and S. Kumar (2013), On the relationship between lightning peak current and Early VLF perturbations, *J. Geophys. Res. Space Physics*, *118*, 7272–7282, doi:10.1002/2013JA019087.
Sentman, D. D., H. C. Stenbaek-Nielsen, M. G. McHarg, and J. S. Morrill (2008), Plasma chemistry of sprite streamers, *J. Geophys. Res.*, *113*, D11112, doi:10.1029/2007JD008941.
Smith, A. K., D. R. Marsh, J. M. Russell III, M. G. Mlynczak, F. J. Martin-Torres, and E. Kyrola (2008), Satellite observations of high nighttime ozone at the equatorial mesopause, *J. Geophys. Res.*, *113*, D17312, doi:10.1029/2008JD010066.
Smith, A. K., D. R. Marsh, M. G. Mlynczak, and J. C. Mast (2010), Temporal variations of atomic oxygen in the upper mesosphere from SABER, *J. Geophys. Res.*, *115*, D18309, doi:10.1029/2009JD013434.

Thomas, L. (1974), Recent developments and outstanding problems in the theory of the D region, *Radio Sci.*, *9*(2), 121–136.
van der Velde, O. A., J. Bór, J. Li, S. A. Cummer, E. Arnone, F. Zanotti, M. Füllekrug, C. Haldoupis, S. NaitAmor, and T. Farges (2010), Multi-instrument observations of a positive gigantic jet produced by a winter thunderstorm in Europe, *J. Geophys. Res.*, *115*, D24301, doi:10.1029/2010JD014442.
Whitten, R. C., and I. G. Poppoff (1962), Associative detachment in the *D* region, *J. Geophys. Res.*, *67*, 1183–1185.
Williams, E., et al. (2012), Resolution of the sprite polarity paradox: The role of halos, *Radio Science*, *47*, RS2002, doi:10.1029/2011RS004794.